Chemical Science

ROYAL SOCIETY OF CHEMISTRY

EDGE ARTICLE

View Article Online
View Journal | View Issue

Cite this: *Chem. Sci.*, 2020, **11**, 3007

All publication charges for this article have been paid for by the Royal Society of Chemistry

Polyoxometalate-based electron transfer modulation for efficient electrocatalytic carbon dioxide reduction†‡

Jing Du, §[a] Zhong-Ling Lang,§[a] Yuan-Yuan Ma, §[ac] Hua-Qiao Tan,*[a] Bai-Ling Liu,[a] Yong-Hui Wang,[a] Zhen-Hui Kang *[b] and Yang-Guang Li *[a]

The electrocatalytic carbon dioxide (CO_2) reduction reaction (CO_2RR) involves a variety of electron transfer pathways, resulting in poor reaction selectivity, limiting its use to meet future energy requirements. Polyoxometalates (POMs) can both store and release multiple electrons in the electrochemical process, and this is expected to be an ideal "electron switch" to match with catalytically active species, realize electron transfer modulation and promote the activity and selectivity of the electrocatalytic CO_2RR. Herein, we report a series of new POM-based manganese-carbonyl (MnL) composite CO_2 reduction electrocatalysts, whereby SiW_{12}–MnL exhibits the most remarkable activity and selectivity for CO_2RR to CO, resulting in an increase in the faradaic efficiency (FE) from 65% (MnL) to a record-value of 95% in aqueous electrolyte. A series of control electrochemical experiments, photoluminescence spectroscopy (PL), transient photovoltage (TPV) experiments, and density functional theory (DFT) calculations revealed that POMs act as electronic regulators to control the electron transfer process from POM to MnL units during the electrochemical reaction, enhancing the selectivity of the CO_2RR to CO and depressing the competitive hydrogen evolution reaction (HER). This work demonstrates the significance of electron transfer modulation in the CO_2RR and suggests a new idea for the design of efficient electrocatalysts towards CO_2RR.

Received 26th October 2019
Accepted 1st February 2020

DOI: 10.1039/c9sc05392a

rsc.li/chemical-science

1. Introduction

The electrocatalytic CO_2 reduction reaction (CO_2RR) that enables the conversion of CO_2 into fuels or value-added organic compounds, along with the storage of intermittent electrical energy, and mitigates the environmental problem, has been regarded as a promising approach to meet future energy demands.[1–4] However, the uncontrolled multiple coupling processes of electron/protons in CO_2RR lead to various reaction pathways, which always generate a number of different products, causing low faradaic efficiency (FE) and selectivity.[5–7] In addition, from the perspective of reaction thermodynamics, the equilibrium potentials for most CO_2RR half-reactions (*e.g.* $CO_2 + 2H^+ + 2e = CO + H_2O$, $E^{\ominus} = -0.11$ V *vs.* RHE, pH = 7) are close to those of the hydrogen evolution reaction (HER) in aqueous electrolyte ($E^{\ominus} = -0.095$ V *vs.* RHE pH = 7), generating an additional competing reaction.[8,9] Nowadays, the regulation of the proton transfer process that occurs in electrocatalytic reactions is considered as an effective means to optimize the reaction pathways, thereby enhancing the product selectivity and faradaic efficiency.[10–13] For example, our previous work demonstrated a design concept for a composite Co_3O_4–CDOts–C_3N_4 electrocatalyst for efficient CO_2 reduction to syngas, where the introduction of CDots with a strong adsorption capacity for H species successfully dominated the proton transfer process and achieved modulation of the reaction pathways of HER and CO_2RR.[14] As another important factor, the electron transfer process has vital influences on the thermodynamics, kinetics and various reaction pathways of the electrocatalytic reaction.[15,16] For instance, the number of transfer electrons can greatly determine the products of the electrocatalytic reaction (*e.g.* CO, 2e; CH_4, 8e). The potential and orientation of electron transfer could also change the reaction pathways. Therefore, quantitative, oriented and controllable electron transfer is expected to be another important strategy in designing efficient electrocatalysts for CO_2 reduction. However, research into this

[a]*Key Laboratory of Polyoxometalate Science of the Ministry of Education, Faculty of Chemistry, Northeast Normal University, Changchun, 130024, China. E-mail: tanhq870@nenu.edu.cn; liyg658@nenu.edu.cn*

[b]*Jiangsu Key Laboratory for Carbon-based Functional Materials and Devices, Institute of Functional Nano and Soft Materials (FUNSOM), Soochow University, Suzhou 215123, China. E-mail: zhkang@suda.edu.cn*

[c]*College of Chemistry and Material Science, Hebei Normal University, Shijiazhuang, Hebei 050024, China*

† This article is dedicated to the memory of our most beloved supervisor Professor En-Bo Wang.

‡ Electronic supplementary information (ESI) available: CCDC 1893118–1893120. For ESI and crystallographic data in CIF or other electronic format see DOI: 10.1039/c9sc05392a

§ These authors have contributed equally.

is still a challenging task since the electron transfers occurring in the catalysts are often complex, fast and undirected, and this makes them difficult to control.

Polyoxometalates (POMs), as a class of well-defined metal-oxo clusters with reversible redox activity, are widely used in electrocatalysis,[15,17–21] photocatalysis,[22–26] and in electrochromism.[27] During these processes, POMs can both accept and release multiple electrons whilst maintaining their structural stability.[17,28] Such a special property can be utilized as a potential "electron switch" to complement the catalytically active species, realize the modulation of the electron transfer pathway in electrochemical reactions, and promote the activity and selectivity of electrocatalytic reactions. In this regard, a manganese carbonyl complex $[Mn^{I}(bipyridyl)(CO)_3Br]$ (MnL) could be an available catalytic species to compete with POMs. As a well-known electrocatalyst for CO_2RR, MnL possesses a clear reaction pathway and can specifically reduce CO_2 to CO in organic solvent.[29–32] However, HER becomes an unavoidable competitive reaction when MnL is used in aqueous electrolyte, due to the rebellious electron transfer process.[33–35] Thus, if POMs can combine with MnL, a new efficient catalyst system may be achieved to modify the electron transfer process and promote the activity and selectivity of the CO_2RR to CO.

Based on the above consideration, we prepared new POM–manganese carbonyl (POM–MnL) composite compounds $[Mn^{I}(bipy)(CO)_3(CH_3CN)]_4(SiW_{12}O_{40})\cdot 5CH_3CN$ (SiW_{12}–MnL), $[Mn^{I}(bipy)(CO)_3(CH_3CN)]_3(PW_{12}O_{40})\cdot 2CH_3CN$ (PW_{12}–MnL), and $[Mn^{I}(bipy)(CO)_3(CH_3CN)]_3(PMo_{12}O_{40})\cdot 2CH_3CN$ (PMo_{12}–MnL) as electrocatalysts to investigate the electrocatalytic CO_2RR. Among these POM–MnL composite catalysts, SiW_{12}–MnL exhibited the most remarkable activity for the CO_2RR to CO with particularly high selectivity, and promotion of the faradaic efficiency (FE) from 65% (MnL) to more than 95% at an overpotential of 0.61 V, which is nearly double that of the parent MnL electrocatalysts in an aqueous electrolyte. A series of electrochemical cyclic voltammetry (CV) tests, photoluminescence spectroscopy (PL) measurements, transient photovoltage (TPV) experiments, and density functional theory (DFT) calculations revealed that the electron transfer process between the POM and MnL units played a key role in modifying the CO_2RR to CO and depressing the competitive HER. Changing the POM species in the composite POM–MnL catalyst system can realize modulation of electron transfer and achieve different improvements on the FE of the CO_2RR.

2. Experimental

2.1 Synthesis of $[Mn^{I}(bipy)(CO)_3(CH_3CN)]_4(SiW_{12}O_{40})\cdot 5CH_3CN$ (abbreviated as SiW_{12}–MnL)

$H_4[\alpha\text{-}SiW_{12}O_{40}]\cdot nH_2O$ (0.72 g, *ca.* 0.25 mmol) was dissolved in 14 mL of water, and 15 mL of acetonitrile (CH_3CN) solution containing $Mn(bipy)(CO)_3Br$ (0.19 g, *ca.* 0.5 mmol) was added dropwise under vigorous stirring. Then, the yellow precipitate appeared immediately. The resulting mixture was stirred for 30 min at room temperature in the dark and was then filtered. The resulting precipitate was collected and dissolved in hot CH_3CN (50 mL), and the orange block crystals were isolated by slow evaporation at 4 °C in the dark after 2–3 days. Yield: 40.4%, based on $Mn(bipy)(CO)_3Br$. Calcd for $C_{70}H_{61}Mn_4N_{17}O_{52}SiW_{12}$ (SiW_{12}–Mn, %): H, 1.43; C, 16.74; N, 5.53; Si, 0.65; Mn, 5.10; W, 51.23. Found (%): H, 1.21; C, 16.85; N, 5.24; Si, 0.72; Mn, 5.32; W, 51.12. FT IR: 2035 (m), 1922 (s) cm^{-1} (CO), 1016 (m), 978 (m), 916 (w), 734 (s) cm^{-1} (SiW_{12}).

2.2 Synthesis of $[Mn^{I}(bipy)(CO)_3(CH_3CN)]_3(PW_{12}O_{40})\cdot 2CH_3CN$ (abbreviated as PW_{12}–MnL)

The synthesis was the same as the aforementioned method, except that $H_3[\alpha\text{-}PW_{12}O_{40}]\cdot nH_2O$ (0.78 g, *ca.* 0.25 mmol) was used to replace $H_4[\alpha\text{-}SiW_{12}O_{40}]\cdot nH_2O$. The final orange block crystals of PW_{12}–MnL possessed a final yield of 0.4 g (*ca.* 60.5%) yield, based on $Mn(bipy)(CO)_3Br$. Calcd for $C_{49}H_{39}Mn_3N_{11}O_{49}PW_{12}$ (PW_{12}–MnL, %): H, 0.99; C, 14.83; N, 3.88; P, 0.78; Mn, 4.15; W, 55.60. Found (%): H, 1.03; C, 14.96; N, 4.05; P, 0.74; Mn, 4.32; W, 56.05. FT-IR: 2038 (m), 1947 (s) cm^{-1} (CO), 1074 (m), 983 (m), 901 (w), 810 (s) cm^{-1} (PW_{12}).

2.3 Synthesis of $[Mn^{I}(bipy)(CO)_3(CH_3CN)]_3(PW_{12}O_{40})\cdot 2CH_3CN$ (abbreviated as PMo_{12}–MnL)

The synthesis was the same as the aforementioned method, except that $H_3[\alpha\text{-}PMo_{12}O_{40}]\cdot nH_2O$ (0.46 g, *ca.* 0.25 mmol) was used to replace $H_4[\alpha\text{-}SiW_{12}O_{40}]\cdot nH_2O$. The final orange block crystals of PMo_{12}–MnL had a yield of 65.1%, based on $Mn(bipy)(CO)_3Br$. Calcd for $C_{49}H_{39}Mn_3Mo_{12}N_{11}O_{49}P$ (PMo_{12}–MnL, %): H, 1.35; C, 20.20; N, 5.29; P, 1.06; Mn, 5.66; Mo, 39.52. Found (%): H, 1.40; C, 20.35; N, 5.12; P, 1.21; Mn, 5.31; Mo, 39.42. FT IR: 2038 (m), 1934 (s) cm^{-1} (CO), 1053 (m), 949 (m), 873 (w), 776 (s) cm^{-1} (PMo_{12}).

2.4 Preparation of the POM–MnL/KB composite electrocatalyst

In order to promote the conductivity of the crystalline POM–MnL composite compounds, Ketjenblack Black (KB) carbon was used as a catalyst carrier to combine with the POM–MnL compounds. Herein, the SiW_{12}–MnL compound was selected as a representative sample to describe the preparation method of POM–MnL/KB. An aliquot of 20 mg KB was added into 20 mL of CH_3CN solution containing 100 mg SiW_{12}–MnL. After sonication for 30 min, the resulting mixture was rotary evaporated to dry and the black powder electrocatalysts (SiW_{12}–MnL loaded on KB) were obtained. The PW_{12}–MnL/KB, PMo_{12}–MnL/KB and parent MnL/KB were prepared in the same way.

2.5 Preparation of CsPOM/KB

The preparation process of CsPOM/KB was as follows. Taking $CsSiW_{12}$ as an example, 0.08 g $Cs_4[\alpha\text{-}SiW_{12}O_{40}]\cdot nH_2O$ and 20 mg KB were mixed in 10 mL of aqueous solution uniformly by ultrasound for 1 hour. Then, the suspension was separated by centrifugation, washed with water three times, and dried in air. The obtained powder was denoted as $CsSiW_{12}$/KB. $CsPW_{12}$/KB and $CsPMo_{12}$/KB were prepared in the same way.

2.6 Preparation of the working electrode

The catalyst suspension was prepared by dispersing 50 mg of POM–MnL/KB or the as-prepared control catalysts (MnL/KB or CsPOM/KB) in 0.5 mL of solution containing 450 μL of absolute ethyl alcohol and 50 μL of 5 wt% Nafion solution, followed by ultrasonication for 1 hour until a homogeneous ink was formed. Then, a 6 μL portion of the as-prepared ink was dropped on the surface of the glassy carbon electrode (0.07065 cm^2), yielding a working electrode after it was dried in air.

2.7 Transient photovoltage measurements

The transient photovoltage (TPV) values were measured on a home-made system, similar to that reported in the literature.[36] The TPV was excited with a nanosecond laser radiation pulse (wavelength of 355 nm and the repetition rate was 5 Hz) from a third harmonic Nd:YAG laser (Beamtech Optronics Co., Ltd.). The TPV signals were amplified by an amplifier and were recorded by an oscilloscope. All measurements were performed at room temperature and under ambient pressure.

3. Results and discussion

3.1 Preparation and characterization of the POM–MnL composite catalysts

All the POM–MnL compounds were synthesized by simple solution self-assembly and crystallization methods. Taking SiW_{12}–MnL as an example, the single crystal of SiW_{12}–MnL was isolated by slow evaporation of the CH_3CN/H_2O solution containing parent $H_4SiW_{12}O_{40}$ and MnL (Scheme S1‡). Single-crystal X-ray diffractions demonstrated that these POM–MnL compounds are composed of a Keggin-type polyoxoanion unit, $[Mn(bipy)(CO)_3(CH_3CN)_3]^+$ moieties and acetonitrile molecules (Fig. S1 and Tables S1–S4‡). The POM unit and MnL species interact with each other by electrostatic (Fig. S2‡) and hydrogen-bonding interactions (Fig. S3, Tables S5–S7‡). The powder X-ray diffraction patterns (PXRD, Fig. S4‡) and thermogravimetric (TG, Fig. S5‡) curves also certified the structural integrity and the composition of the crystalline POM–MnL catalysts. Moreover, these POM–MnL complexes were soluble in acetonitrile but were insoluble in water and exhibited excellent stabilities in 0.5 M CO_2-saturated $KHCO_3$ solution (Fig. S6 and S7‡), implying their potential application in the heterogeneous CO_2RR in aqueous electrolytes.

To promote the electroconductivity of crystalline POM–MnL catalysts for succeeding in the electrocatalytic investigations, Ketjenblack (KB) carbon was introduced into the CH_3CN solution of POM–MnL. After evaporating the solution to dryness, POM–MnL loaded on KB (POM–MnL/KB) heterogeneous composites were achieved (Scheme S1‡). The composition and morphological features of such composite materials were characterized by transmission electron microscopy (TEM). As shown in Fig. 1a and S8a, S9a,‡ POM–MnL compounds are uniformly distributed on *ca.* 30 nm KB nanospheres, and no obvious aggregation was observed. High-resolution TEM images (the inset of Fig. 1a and S8a, S9a‡) reveal that the average size of a POM–MnL nano-crystal is about 1.5 nm. Furthermore, elemental mapping images of POM–MnL/KB in Fig. 1b–g, S8b–g and S9b–g‡ display the homogeneous distribution of C, O, Mn, Si/P and W/Mo in the whole composites. Energy dispersive X-ray absorption (EDX) analyses (Fig. 1h and S10‡) also confirm the composition of POM–MnL/KB, and the contents of SiW_{12}–MnL, PW_{12}–MnL, and PMo_{12}–MnL in POM–MnL/KB are about 81.85%, 85.64% and 86.61%, respectively. Moreover, X-ray photoelectron spectroscopy (XPS) of the POM–MnL/KB composites was also carried out to elucidate their valence states and compositions. As observed in Fig. 1i, j and S11,‡ the XPS spectra of POM–MnL/KB indicated the presence of C, N, O, Si/P and W/Mo in the catalysts. In SiW_{12}–MnL/KB, the high-resolution W 4f spectrum features two characteristic peaks at 36.1 and 38.69 eV, which can be assigned to W^{VI} $4f_{7/2}$ and $4f_{5/2}$ in the SiW_{12} species,[37] and this coincides with the BVS calculation results (Table S8‡).[38] The Mn 2p XPS exhibits two peaks at 641.8 and 653.0 eV, which can be ascribed to Mn^I $2p_{3/2}$ and $2p_{1/2}$, respectively.[39] For PW_{12}–MnL/KB and PMo_{12}–MnL/KB, the XPS spectra of W and Mo also demonstrated congruent results with BVS calculations (Fig. S12 and Table S9‡).[40,41] In addition, Fourier transform infrared (FT-IR) spectra of POM–MnL/KB displayed the characteristic vibrations of POM and MnL, further certifying the composition of the POM–MnL/KB materials (Fig. S13‡). Furthermore, the Brunauer–Emmett–Teller (BET) surface areas of SiW_{12}–MnL/KB, PW_{12}–MnL/KB and PMo_{12}–MnL/KB, calculated by the N_2 isotherms, were 143.7, 105.4 and 153.3 $m^2\ g^{-1}$ (Fig. S14‡), respectively. The high surface area can efficiently facilitate charge transfer and expose more active sites. Moreover, the H^+ adsorption experiments revealed that the amount of adsorbed H^+ was 133.53 mg mol^{-1} for SiW_{12}–MnL and 14.73 mg mol^{-1} for MnL, signifying that the introduction of POMs can provide a sufficient source of H^+ for the reduction of CO_2 in the center of MnL.[14] All the above results demonstrate that the POM–MnL/KB composite catalyst systems are successfully synthesized for the electrocatalytic CO_2RR investigation.

3.2 The electrocatalytic CO_2RR performance of POM–MnL

Before the electrocatalytic CO_2RR investigation, the electrochemical properties of free POMs as well as MnL in solution, the cesium salt of POMs loaded on KB (CsPOM/KB) and POM–MnL/KB were studied by cyclic voltammetry (CV) experiments. The CVs of the free POM species ($H_4SiW_{12}O_{40}$, $H_3PW_{12}O_{40}$ and $H_3PMo_{12}O_{40}$) were measured in H_2SO_4 electrolyte, and free MnL was measured in $KHCO_3$ electrolyte. As shown in Fig. S15,‡ three Keggin-type POMs exhibit similar three pairs of characteristic redox peaks that are assigned to the four-electron redox behavior of W^{VI}/W^V or Mo^{VI}/Mo^V in POMs.[42,43] The CV of MnL in $KHCO_3$ solution shows two obvious reduction peaks at 0.27 V and −0.46 V *vs.* RHE (Fig. S15d‡). The peak at 0.27 V can be ascribed as reduction of the ligand in MnL to generate the $[Mn(L^-)(CO)_3Br]^-$ species, and the peak at −0.46 V can be attributed to the departure of Br^- in MnL to generate a catalytically active species, $[Mn(L)(CO)_3]^-$.[32,34] It is noteworthy that the redox peak potentials of these three POMs display clear

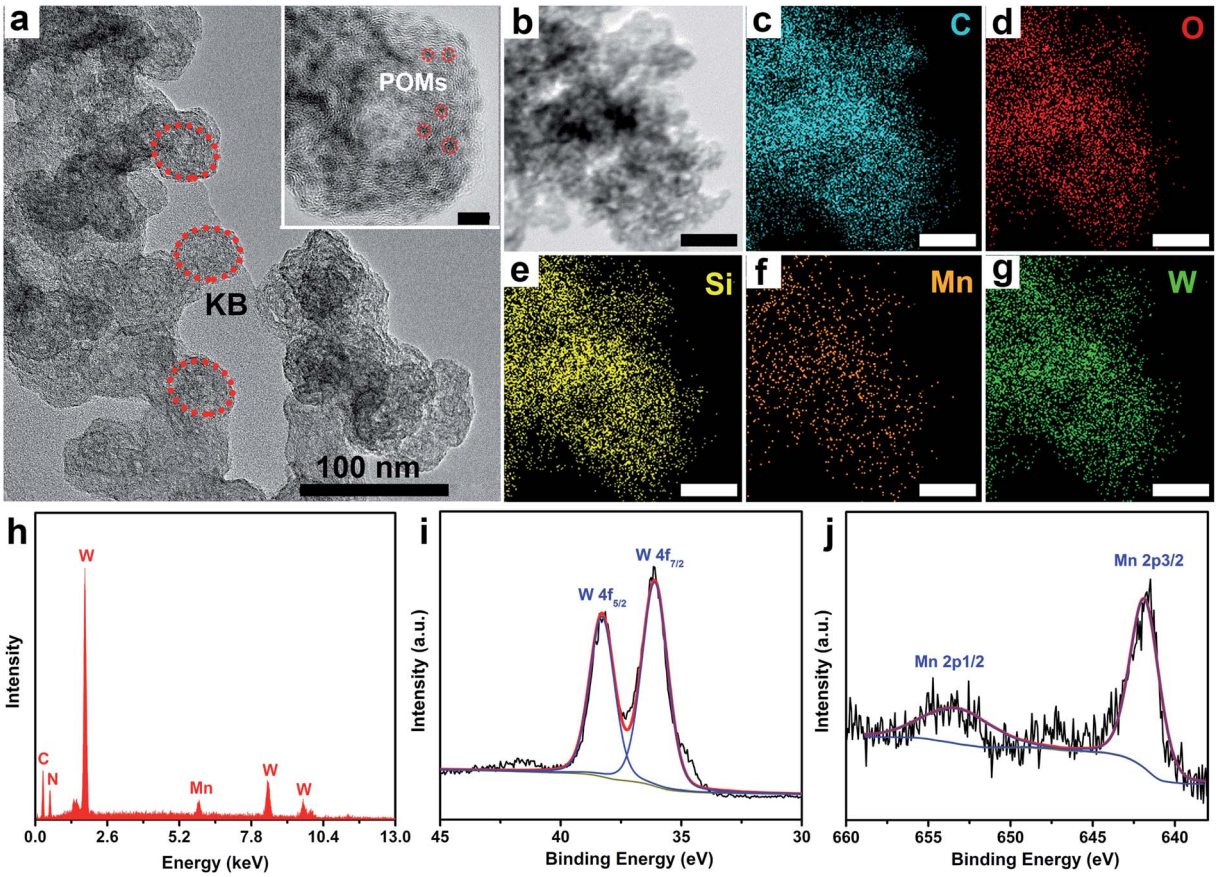

Fig. 1 (a) TEM images of SiW_{12}–MnL/KB (inset: HR-TEM images of SiW_{12}–MnL/KB, scale bar: 5 nm). (b–g) Corresponding elemental mapping of C, O, Si, Mn and W of SiW_{12}–MnL/KB, scale bar: 100 nm. (h) The EDX spectra of SiW_{12}–MnL/KB. (i and j) The XPS spectra of SiW_{12}–MnL/KB: (i) W, (j) Mn.

deviations, which may endow the POMs with different electron storage and transfer properties.

After POMs and MnL were loaded on KB, the electrochemical properties did not show much change (Fig. 2a and S16‡). MnL/KB showed two reduction peaks at 0.28 V and −0.45 V *vs.* RHE, which is consistent with the reduction potential of free MnL in solution. Three CsPOMs/KB composites also exhibited electrochemical redox signals similar to free POMs in solution. The reduction peaks of $CsSiW_{12}$/KB were located at 0.40, 0.14, −0.21 and −0.38 V *vs.* RHE, the reduction peaks of $CsPW_{12}$/KB were located at 0.46 and −0.42 V *vs.* RHE and the reduction peaks of $CsPMo_{12}$/KB were located at 0.30 and −0.51 V *vs.* RHE. In comparison with the CVs of free POM in solution, it can be observed that the reduction peak potentials of the CsPOMs/KB composites are slightly offset compared with those of free POM in solution, and this may be due to the increase in pH in solution.[44] The reversibility of the electrochemical redox peak becomes worse, and this may be due to the changes of the microenvironments of the surface after POM immobilization on KB.[45,46] It is worth noting that the reduction peaks of CsPOM/KB are clearly more positive than those of MnL (−0.45 V), indicating that the polyoxoanions preferentially obtain electrons.

Meanwhile, for POM–MnL/KB, the reduction peaks at 0.25 and −0.03 V for SiW_{12}–MnL/KB, 0.12 V for PW_{12}–MnL/KB and 0.24 V for PMo_{12}–MnL/KB result from the electron storage of POM (Fig. 2a and S16‡). These reduction peaks move towards a negative potential compared to those of CsPOM/KB, and this may be related to the difference in their cations.[47] The reduction peaks at *ca.* −0.46 V for SiW_{12}–MnL/KB, −0.42 V for PW_{12}–MnL/KB and −0.65 V for PMo_{12}–MnL/KB become strong and broad, and this may be due to the overlap of the last reduction peak of POMs and MnL. This endows electron transfer to occur between POMs and MnL. Furthermore, the CVs of POM–MnL/KB at different scan rates from 25 to 125 mV s^{-1} have also been carried out. The last pair of redox peak currents are plotted in Fig. S17–S19‡ *vs.* the square root of the scan rates ($v^{1/2}$), indicating that the electrochemical process is a diffusion-controlled process.[48,49]

To affirm the CV results, a series of density functional theory (DFT) calculations were conducted using the standard B3LYP functional to explore the electron store and transfer behaviour in the electrochemical process of the POM–MnL composite. In Fig. 2b the orbital energies and composition of POM–MnL are compared with the free MnL species. It is worth noting that the involvement of POMs induces a clearly different lowest unoccupied molecular orbital (LUMO), which has complete participation of the W(4d) and O(2p) orbitals from POM, whereas the main contributions are from bipy in pure MnL. This implies

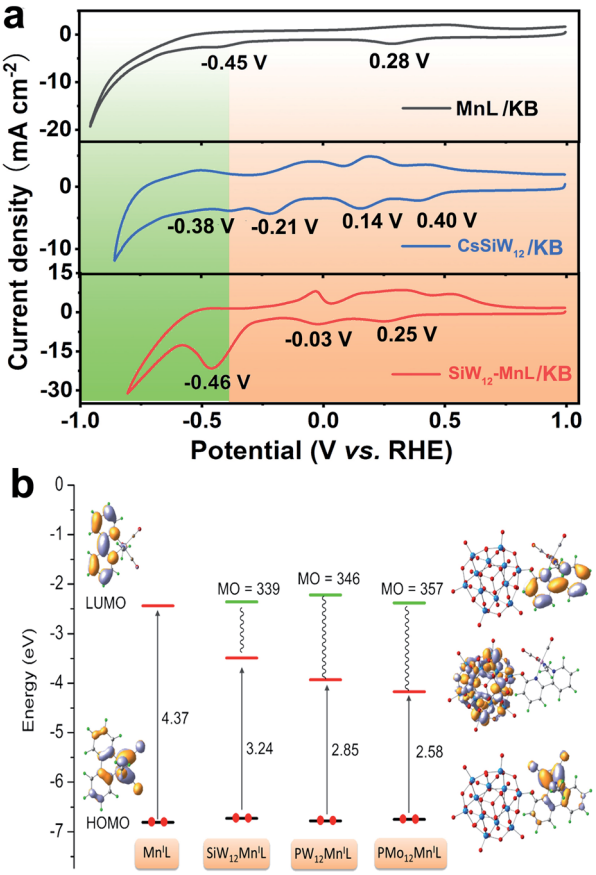

Fig. 2 (a) The CVs for MnL/KB, $CsSiW_{12}$/KB and SiW_{12}–MnL/KB in 0.5 mol L^{-1} N_2-saturated $KHCO_3$ at a 0.05 V s^{-1} scan rate. (b) Computed frontier orbitals (compositions and energies) for MnL, SiW_{12}–MnL, PW_{12}–MnL, and PMo_{12}–MnL (the green lines represent the unoccupied molecular orbitals (MO) contributed by MnL in POM–MnL).

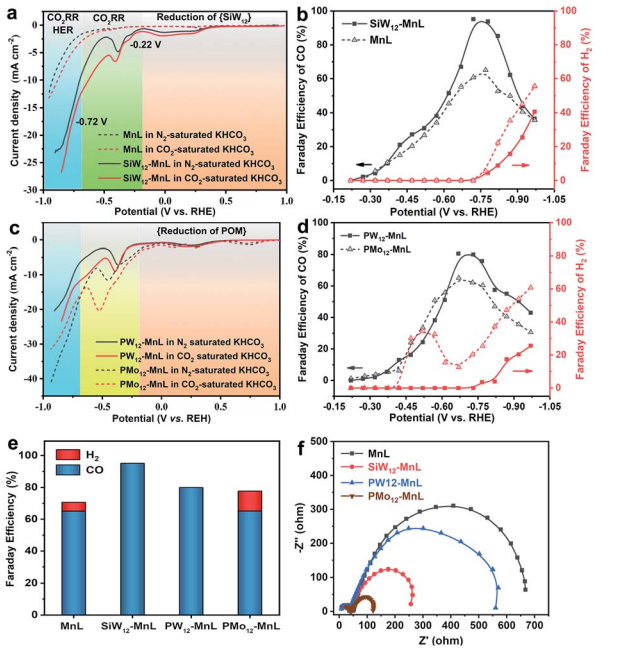

Fig. 3 (a) The LSV curves of SiW_{12}–MnL/KB and MnL/KB in 0.5 M N_2-(black curve) or CO_2-(red curve) saturated $KHCO_3$ electrolyte. (b) The FE of CO at different potentials for MnL/KB and SiW_{12}–MnL/KB (the line is drawn only to guide the eye). (c) The LSV curves of PW_{12}–MnL/KB and Pmo_{12}–MnL/KB in 0.5 M N_2-(black curve) or CO_2-(red curve) saturated $KHCO_3$ electrolyte. (d) The FE of CO at different potentials for PW_{12}–MnL/KB and PMo_{12}–MnL/KB (the line is drawn only to guide the eye). (e) The FE values of CO and H_2 at the overpotential of the highest FE of CO for MnL/KB and POM–MnL/KB. (f) Nyquist plots of electrochemical impedance spectra (EIS) of MnL/KB and POM–MnL/KB in CO_2-saturated 0.5 M $KHCO_3$ aqueous solution.

that the electrons will preferentially be localized on the POM units in the electrochemical reduction process. Only when the LUMO orbit of the POM is filled with electrons can the electrons on the SiW_{12} be transferred to the MnL component, and at this point the MnL component begins to be reduced. Such a calculation indicates that the POM is reduced first and then transfers electrons to MnL during the electrochemical process.

Subsequently, the electrocatalytic CO_2RR performance of POM–MnL/KB was investigated (Fig. 3 and S20‡). As shown in Fig. 3a, the polarization curves of SiW_{12}–MnL/KB in CO_2-saturated 0.5 M $KHCO_3$ can be divided into three parts. Firstly, the reduction peaks in the potential range of 1.0 to −0.22 V *vs.* RHE can be attributed to the reduction of the SiW_{12} polyoxoanion. In this range, no H_2 or CO can be detected (Fig. 3b). Secondly, a broad cathodic wave within the scope of −0.22 to −0.46 V *vs.* RHE may be caused by the mixed process of the electron storage and transfer from POM to MnL, generating the CO_2RR active species. Within this potential range, only CO was detected, and its Faraday efficiency slowly increased with the negative potential scans. In the range of −0.46 to −0.72 V *vs.* RHE, a sharp increase in the reduction current density was observed, and this is caused by the CO_2RR. The corresponding FE of CO increases with the increase in applied potential and reaches a maximum of ~95% at −0.72 V *vs.* RHE. Thirdly, as the potential continues to negatively sweep beyond −0.72 V *vs.* RHE, the current density displays a continuous increase with a higher slope, implying that the electrochemical reaction pathways have been changed and some competing reaction may occur. Compared with MnL/KB (Fig. 3a and b), SiW_{12}–MnL/KB remarkably enhances the Faraday efficiency of CO (from 65% to a record 95% at −0.72 V *vs.* RHE), and reduces the Faraday efficiency of H_2 (from 59% to 39% at −1.0 V *vs.* RHE) in CO_2-saturated $KHCO_3$ electrolyte. This result indicates that the electron store and transfer behavior between the POM and MnL units could promote the reaction pathway of the CO_2RR into CO, and inhibit the HER reaction pathway, thus enhancing the FE and selectivity for CO.

To deeply understand the significant role of POMs, the electrochemical CO_2RR performances of PW_{12}–MnL/KB and PMo_{12}–MnL/KB were also investigated. As depicted in Fig. 3c, both PW_{12}–MnL/KB and PMo_{12}–MnL/KB exhibit similar electron storage, electron transfer, CO_2RR and HER electrochemical processes as SiW_{12}–MnL/KB. However, since different POM species exhibit different redox activities, the PW_{12} and PMo_{12} polyoxoanions in POM–MnL have different electron transfer capacities, resulting in different FEs of H_2 and CO. Definitvely,

PW_{12}–MnL/KB can specifically catalyze the reduction of CO_2 into CO until the applied potential reaches −0.72 V *vs.* RHE, then the maximum CO FE of 80% is achieved. After −0.72 V *vs.* RHE, the CO_2RR process is accompanied by the generation of H_2 (Fig. 3d). This phenomenon is similar to that of SiW_{12}–MnL/KB, implying that similar electron storage and transfer behaviors occur between PW_{12} and the MnL unit. As for PMo_{12}–MnL/KB, the H_2 generation and CO_2RR processes occurred simultaneously (Fig. 3d), revealing that the PMo_{12} and MnL units work synchronously as HER and CO_2RR active centers. Notably, when the applied potential reaches −0.52 V *vs.* RHE, the FE of H_2 shows an apparent downwards trend while the FE of CO still increases. The maximum CO FE of 65% could be achieved at −0.64 V *vs.* RHE, accompanied by a 12% FE of the by-product H_2. In the electrochemical process catalyzed by PMo_{12}–MnL/KB, two reaction pathways (CO_2RR and HER) occur simultaneously, and this is remarkably distinct to the processes of SiW_{12}–MnL/KB and PW_{12}–MnL/KB (Fig. 3e). This result is possibly due to the difficult electron transfer from the PMo_{12} unit to MnL, resulting in the electrons being stored on PMo_{12} for the competitive HER. Overall, the above results suggest that the combination of SiW_{12} and PW_{12} with the MnL species facilitates electron transfer from POM to the MnL center, and that this accelerates the generation of active Mn sites, promotes the CO_2RR pathway, and inhibits the HER pathway, further ensuring the high efficiency and selectivity of the CO_2RR. Meanwhile, due to the difficult electron transfer from PMo_{12} to the MnL center, the stored-electrons on the PMo_{12} unit in turn facilitate the evolution of H_2, which is unfavorable to the CO_2 process, leading to the low efficiency and selectivity of the CO_2RR. Therefore, the reaction pathway, Faraday efficiency (FE) and selectivity of the electrocatalytic reaction could be regulated by modulating the electron transfer behavior between the POMs and MnL.

The geometric-corrected current density and partial current density for CO (j_{CO}) of the POM–MnL composites were investigated (Fig. S21‡). As shown in Fig. S21,‡ the induction of POM significantly enhanced the current density and the j_{CO} value of MnL. The j_{CO} values of SiW_{12}–MnL/KB at −0.72 V *vs.* RHE are almost more than twice those of MnL/KB. Moreover, we further measured the electrochemical real surface areas (ECSA) of POM–MnL/KB and MnL/KB. Fig. S22‡ shows that POM–MnL/KB and MnL/KB have similar double-layer capacitance values (9.25 mF cm^{-2} for SiW_{12}–MnL/KB, 6.92 mF cm^{-2} for PW_{12}–MnL/KB, 7.10 mF cm^{-2} for PMo_{12}–MnL/KB, and 7.20 mF cm^{-2} for MnL/KB), suggesting that these catalysts possess considerable surface areas. Then, we normalized the current density and j_{CO} at −0.72 V *vs.* RHE for the POM–MnL/KB and MnL/KB catalysts by the electrochemical active surface area (ECSA), to provide more convincing certification for the intrinsic activity and exclude the effect of surface area on the activity (Fig. S23‡). Fig. S23‡ demonstrates the ECSA-corrected current density and j_{CO} at −0.72 V *vs.* RHE of the SiW_{12}–MnL/KB catalysts, which show an almost 1.9 times increment compared to those of the MnL/KB catalyst, thus directly demonstrating the higher intrinsic CO_2RR activity of POM–MnL without including the effects of the surface area. In addition, because the active center for the catalytic CO_2 reduction is on the MnL component, the MnL surface concentration of POM–MnL/KB can be calculated by ICP and EDX results. The surface content of MnL was 1.36 mg cm^{-2} in MnL/KB, 0.61 mg cm^{-2} in SiW_{12}–MnL/KB, 0.51 mg cm^{-2} in PW_{12}–MnL/KB and 0.70 mg cm^{-2} in PMo_{12}–MnL/KB, and the mass activities of POM–MnL/KB and MnL/KB were also evaluated by normalizing the current density and j_{CO} at −0.72 V *vs.* RHE with the amount of active center MnL (Fig. S24‡). The SiW_{12} species boosted the mass activity of MnL by almost 5 times. Overall, the selectivity and activity of the POM–MnL catalysts in an aqueous electrolyte were quite enhanced after regulation of the electron transfer by POMs.

Moreover, the electron transfer process in the CO_2RR reaction was also confirmed by electrochemical impedance spectroscopy (EIS). Fig. 3f presents the EIS spectra of MnL/KB, PW_{12}–MnL/KB, SiW_{12}–MnL/KB and PMo_{12}–MnL/KB. The equivalent circuit model[50] shown in Fig. S25‡ was selected to simulate the electrochemical impedance data and the simulated values of the equivalent circuit components are shown in Table S10.‡ Since the electrochemical impedance experiments were performed in the same electrolyte, and all of them used highly conductive KB, POM–MnL/KB and MnL/KB exhibited similar electrolyte resistance and electronic resistance. It was found that after introducing PW_{12} and SiW_{12} polyoxoanions into MnL, the mass transfer impedance values clearly decreased, and this may arise from the improvement of the electrocatalytic activity of MnL after the introduction of POMs. Compared to SiW_{12}–MnL and PW_{12}–MnL, the introduction of the PMo_{12} polyoxoanion induced two kinds of reaction pathways (the reduction of CO_2 into CO and HER) during the CO_2RR, endowing PMo_{12}–MnL/KB with the smallest mass transfer impedance among these POM–MnL composites. Such results further suggest that the electron transfer behaviors between POMs and MnL could significantly affect the electrochemical reactions.[51] These results further demonstrate the significant role (electron-transfer-modulator) of POM species in the enhancement of the CO_2RR performance of MnL.

In addition, SiW_{12}–MnL/KB exhibits satisfactory long-term stability for sustained CO_2RR electrocatalysis. Its chronoamperometric (*i*–*t*) curve response at −0.72 V *vs.* RHE (η = 0.61) was continuously monitored for 12 h. The negligible activity decay was observed (Fig. S26‡). Furthermore, the IR spectrum and TEM images of SiW_{12}–MnL/KB after the 12 h electrolysis further confirmed the good stability of SiW_{12}–MnL/KB in terms of the negligible structural and morphological differences (Fig. S27 and S28‡).

3.3 Mechanism of POM–MnL catalyzed CO_2 reduction

The aforementioned experimental results showed that the FE and selectivity of CO_2 reduction could be controlled by the electron storage and transfer capacities of different POMs. However, the electron transfer behavior is usually quick and difficult to characterize during electrocatalysis, therefore DFT calculations were used to illustrate the possible electron transfer process of the POM–MnL catalyst in electrocatalysis. The 2e, 3e, 4e, and 5e electronic reduction processes for SiW_{12}–MnL

and the electronic configurations were simulated and are provided in Fig. 4a. This reveals that the SiW_{12} polyoxoanion could accept up to four electrons in the electrochemical process to achieve the highly reduced state SiW_{12}–MnL. Once POM–MnL undergoes electrochemical reduction of three electrons and above (four or five electrons, Fig. 4a), CH_3CN on the MnL unit could be released spontaneously, and one- or two-electron transfer from POM to MnL occurred. At this point, the MnL component begins to form the active species center ($[Mn(bpy)(CO)_3]^+$) of the CO_2 reduction. Specifically, the SiW_{12} unit is the easiest to transfer two electrons to the MnL component to form 2e-reduced active centers (-22.9 kcal mol^{-1} for CH_3CN releasing), whereas only one electron is transferred in the presence of PMo_{12} based on the 5e-reduction state, indicating that PMo_{12} is the most difficult to transfer electrons to MnL. Such results indicate that the POM species are easier to acquire electrons than MnL during the electrochemical reduction and deliver electrons to the MnL unit for further catalytic CO_2RR, exerting a significant effect on the modulation of electron transfer (Scheme 1). To verify the computational results, solid-state fluorescence spectroscopy and transient photovoltage (TPV) measurements were carried out to explore the electron transfer behaviour in POM–MnL. As shown in Fig. S29,‡ a distinct fluorescence quenching was observed after introducing POMs into MnL, further confirming the existence

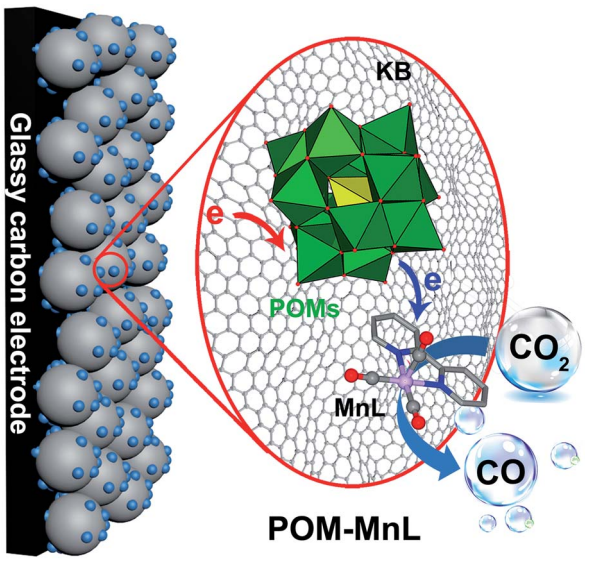

Scheme 1 Schematic diagram of the reaction mechanism induced by POM–MnL.

of an electron transfer interaction between the POMs and MnL.[52] Next, the transient photovoltage (TPV) technique was applied to investigate the electron transfer behavior of POMs in the composite electrocatalysts.

As depicted in Fig. 4b, the POM–MnL composite catalysts exhibited longer photovoltage decay times than that of MnL. Such a prolonged photovoltage decay lifetime was caused by the electron transfer process from the electron-stored POMs to MnL, and this is consistent with the electrochemical CV and DFT calculation results. A broad shoulder peak (at 5 ms) appears in the photovoltage decay curve of POM–MnL, which is caused by the storage of electrons by POMs. Notably, different POM species in the POM–MnL composite catalysts also lead to different degrees of photovoltage decay lifetime prolongation, further indicating that these POMs have different electron-storage capacities and electron-transfer modulation capabilities. Therefore, SiW_{12}–MnL displays the longest photovoltage decay lifetime, indicating the electron transfer between SiW_{12} and MnL unit is more favorable. Meanwhile, PMo_{12}–MnL showed the shortest photovoltage decay lifetime, suggesting that the PMo_{12} unit is the least susceptible to electron transfer with MnL. The TPV curves of POM–MnL and MnL loaded on KB in the N_2-saturated $KHCO_3$ aqueous solution were also studied. As shown in Fig. S30‡, the behavior of the photovoltage decay of these catalysts in solution is similar to that of the solid samples, indicating that the electron-storage and electron-transfer modulation by POM also exist in the solution system. The above results indicate that the FE and selectivity of electrocatalytic CO_2 reduction can be promoted when POMs facilitate electron transfer to MnL.

From the energy aspect, H^+ binding and CO_2 activation on the active MnL and SiW_{12}–MnL catalysts, respectively, were also considered. As illustrated in Fig. 5, the energy barriers for protonation of SiW_{12}–MnL and MnL were calculated to 18.3 and

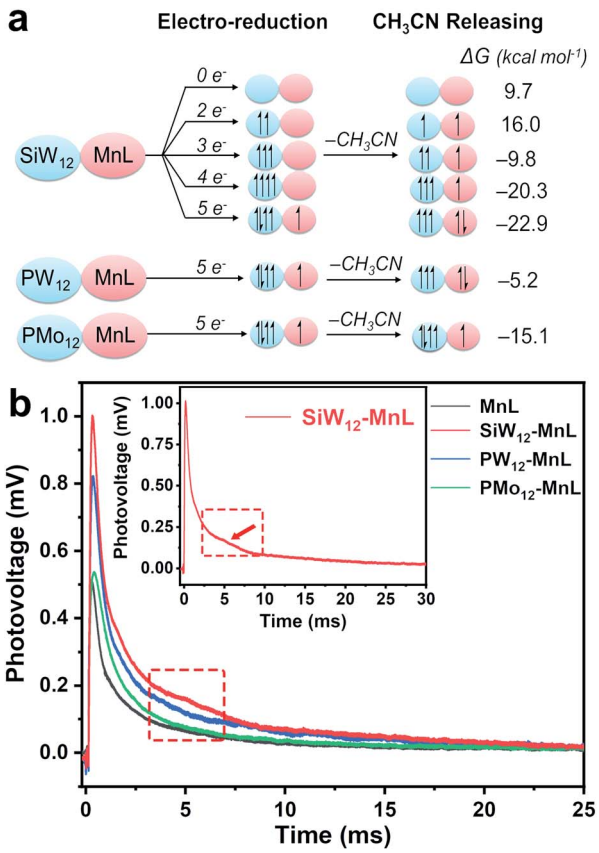

Fig. 4 (a) The electronic configurations for the different reduction degree states of SiW_{12}–MnL, SiW_{12}–MnL, PW_{12}–MnL, and PMo_{12}–MnL. (b) The transient photovoltage curves of powder POM–MnL and MnL.

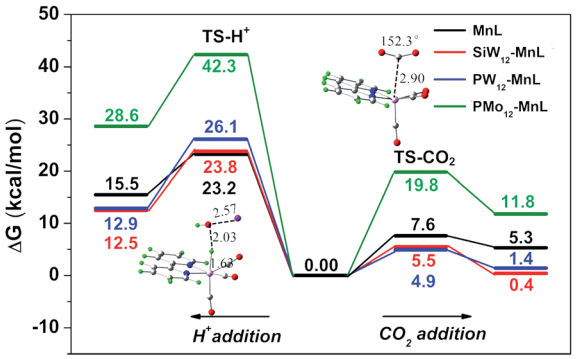

Fig. 5 Potential energy surfaces for H^+ and CO_2 addition to the respective active CO_2 and H adducts.

16.6 kcal mol^{-1}, which are higher than those for CO_2 activation. It can be seen that the pure MnL itself represents a certain selectivity for CO_2 reduction; the combination with the SiW_{12} polyoxoanion further increases the energy differences between proton affinity and CO_2 activation. We have addressed two main contributions to the differences: the slightly increased protonation barrier (23.2 *vs.* 23.8 kcal mol^{-1}) and the clearly decreased CO_2 activation barrier (7.6 *vs.* 5.5 kcal mol^{-1}). Consequently, less competition between CO_2 reduction and H_2 evolution is achieved computationally for the POM-involved system, and this coincides well with the experimental results. The catalytic selectivity is also dependent on the composition of the POMs. Similar trends have been obtained in the PW_{12}–MnL case as in SiW_{12}–MnL. However, the CO_2 adduct is calculated to 1 kcal mol^{-1} less stable in PW_{12}–MnL than in SiW_{12}–MnL, which may slightly decrease its selectivity for CO_2 reduction as shown in the experiments. Surprisingly, the addition of CO_2 on PMo_{12}–MnL, as well as the activated barrier, is much higher than the others, significantly limiting its activity. Therefore, the electron transfer from the POM unit to the MnL center may also affect the adsorption process of the reaction substrate in the MnL center, changing the FE and selectivity of the CO_2RR.

4. Conclusion

In summary, we fabricated a series of POM–MnL composite electrocatalysts and demonstrated an electron-transfer-modulation strategy for obtaining highly efficient electrocatalysts towards the CO_2RR. Electrochemical, photoluminescence spectroscopy, transient photovoltage experiments and DFT calculations demonstrated that the electron transfer from POM to MnL could be used to prompt the electrocatalytic activity, FE and selectivity of CO_2 reduction. Among them, SiW_{12}–MnL exhibited excellent electron-transfer regulation behaviour, and superior CO_2RR activity with particularly high selectivity, more than 95% FE at an overpotential of 0.61 V *vs.* RHE, and prominent stability of 12 h. This work reveals the role of POMs in optimizing the electron transfer pathway during electrocatalytic reactions, and provides a new perspective to designing highly efficient and selective catalysts for crucial electrocatalytic reactions.

Conflicts of interest

There are no conflicts to declare.

Acknowledgements

This work is supported by the National MCF Energy R&D Program (2018YFE0306105), Innovative Research Group Project of the National Natural Science Foundation of China (51821002), Natural Science Foundation of Jiangsu Province (BK20190041, BK20190828), Key-Area Research and Development Program of GuangDong Province (2019B010933001), the Collaborative Innovation Center of Suzhou Nano Science & Technology, the Priority Academic Program Development of Jiangsu Higher Education Institutions (PAPD), the 111 Project, National Natural Science Foundation of China (21771033, 21671036, 51422207, 51972216, 51725204, 21771132, 51572179, 51132006, 21901060, and 21901035), the Fundamental Research Funds for the Central Universities (2412018BJ001, 2412018ZD007 and 2412018QD005), the Scientific Development Project of Jilin Province (20190201206JC), the Foundation of Jilin Educational Committee (JJKH20190268KJ), the Specialized Research Fund for the Doctoral Program of Higher Education (20123201110018) and the Opening Project of Key Laboratory of Polyoxometalate Science of Ministry of Education. The computational work was carried out at the LvLiang Cloud Computing Center of China, and the calculations were performed on TianHe-2.

References

1 T. Burdyny and W. A. Smith, *Energy Environ. Sci.*, 2019, **12**, 1442.
2 S. Liu, X. F. Lu, J. Xiao, X. Wang and X. W. Lou, *Angew. Chem., Int. Ed.*, 2019, **58**, 13828.
3 N. Han, Y. Wang, L. Ma, J. Wen, J. Li, H. Zheng, K. Nie, X. Wang, F. Zhao, Y. Li, J. Fan, J. Zhong, T. Wu, D. J. Miller, J. Lu, S.-T. Lee and Y. Li, *Chem*, 2017, **3**, 652.
4 C. Li, X. Tong, P. Yu, W. Du, J. Wu, H. Rao and Z. M. Wang, *J. Mater. Chem. A*, 2019, **7**, 16622.
5 D. Voiry, H. S. Shin, K. P. Loh and M. Chhowalla, *Nat. Rev. Chem.*, 2018, **2**, 0105.
6 S. Liu, J. Xiao, X. F. Lu, J. Wang, X. Wang and X. W. Lou, *Angew. Chem., Int. Ed.*, 2019, **58**, 8499.
7 J. Hussain, H. Jonsson and E. Skulason, *ACS Catal.*, 2018, **8**, 5240.
8 D. D. Zhu, J. L. Liu and S. Z. Qiao, *Adv. Mater.*, 2016, **28**, 3423.
9 F. Quan, G. Zhan, H. Shang, Y. Huang, F. Jia, L. Zhang and Z. Ai, *Green Chem.*, 2019, **21**, 3256.
10 X. Zheng, Y. Ji, J. Tang, J. Wang, B. Liu, H.-G. Steinrück, K. Lim, Y. Li, M. F. Toney, K. Chan and Y. Cui, *Nat. Catal.*, 2018, **2**, 55.
11 B. Yan, R. P. Bisbey, A. Alabugin and Y. Surendranath, *J. Am. Chem. Soc.*, 2019, **141**, 11115.
12 Y. Y. Ma, Z. L. Lang, L. K. Yan, Y. H. Wang, H. Q. Tan, K. Feng, Y. J. Xia, J. Zhong, Y. Liu, Z. H. Kang and Y. G. Li, *Energy Environ. Sci.*, 2018, **11**, 2114.

13 T. Huang, E. S. Rountree, A. P. Traywick, M. Bayoumi and J. L. Dempsey, *J. Am. Chem. Soc.*, 2018, **140**, 14655.
14 S. Guo, S. Zhao, X. Wu, H. Li, Y. Zhou, C. Zhu, N. Yang, X. Jiang, J. Gao, L. Bai, Y. Liu, Y. Lifshitz, S. T. Lee and Z. Kang, *Nat. Commun.*, 2017, **8**, 1828.
15 Y. R. Wang, Q. Huang, C. T. He, Y. Chen, J. Liu, F. C. Shen and Y. Q. Lan, *Nat. Commun.*, 2018, **9**, 4466.
16 A. Dutta, A. Kuzume, V. Kaliginedi, M. Rahaman, I. Sinev, M. Ahmadi, B. Roldán Cuenya, S. Vesztergom and P. Broekmann, *Nano Energy*, 2018, **53**, 828.
17 B. Rausch, M. D. Symes, G. Chisholm and L. Cronin, *Science*, 2014, **345**, 1326.
18 R. Liu, G. Zhang, H. Cao, S. Zhang, Y. Xie, A. Haider, U. Kortz, B. Chen, N. S. Dalal, Y. Zhao, L. Zhi, C.-X. Wu, L.-K. Yan, Z. Su and B. Keita, *Energy Environ. Sci.*, 2016, **9**, 1012.
19 R. Liu, K. Cao, A. H. Clark, P. Lu, M. Anjass, J. Biskupek, U. Kaiser, G. Zhang and C. Streb, *Chem. Sci.*, 2020, **11**, 1043.
20 S. J. Folkman, J. Soriano-Lopez, J. R. Galan-Mascaros and R. G. Finke, *J. Am. Chem. Soc.*, 2018, **140**, 12040.
21 H. B. Wu, B. Y. Xia, L. Yu, X. Y. Yu and X. W. Lou, *Nat. Commun.*, 2015, **6**, 6512.
22 X. B. Han, Y. G. Li, Z. M. Zhang, H. Q. Tan, Y. Lu and E. B. Wang, *J. Am. Chem. Soc.*, 2015, **137**, 5486.
23 J. Ettedgui, Y. Diskin-Posner, L. Weiner and R. Neumann, *J. Am. Chem. Soc.*, 2011, **133**, 188.
24 A. M. Khenkin, I. Efremenko, L. Weiner, J. M. L. Martin and R. Neumann, *Chem.–Eur. J.*, 2010, **16**, 1356.
25 S. M. Lauinger, J. M. Sumliner, Q. Yin, Z. Xu, G. Liang, E. N. Glass, T. Lian and C. L. Hill, *Chem. Mater.*, 2015, **27**, 5886.
26 K. P. Sullivan, M. Wieliczko, M. Kim, Q. Yin, D. L. Collins-Wildman, A. K. Mehta, J. Bacsa, X. Lu, Y. V. Geletii and C. L. Hill, *ACS Catal.*, 2018, **8**, 11952.
27 B. Zhang, W. Guan, S. Zhang, B. Li and L. Wu, *Chem. Commun.*, 2016, **52**, 5308.
28 L. MacDonald, J. C. McGlynn, N. Irvine, I. Alshibane, L. G. Bloor, B. Rausch, J. S. J. Hargreaves and L. Cronin, *Sustainable Energy Fuels*, 2017, **1**, 1782.
29 G. Neri, J. J. Walsh, G. Teobaldi, P. M. Donaldson and A. J. Cowan, *Nat. Catal.*, 2018, **1**, 952.
30 J. A. Keith, K. A. Grice, C. P. Kubiak and E. A. Carter, *J. Am. Chem. Soc.*, 2013, **135**, 15823.
31 S. Sung, D. Kumar, M. Gil-Sepulcre and M. Nippe, *J. Am. Chem. Soc.*, 2017, **139**, 13993.
32 M. Bourrez, F. Molton, S. Chardon-Noblat and A. Deronzier, *Angew. Chem., Int. Ed.*, 2011, **50**, 9903.
33 A. Sinopoli, N. T. La Porte, J. F. Martinez, M. R. Wasielewski and M. Sohail, *Coord. Chem. Rev.*, 2018, **365**, 60.
34 J. J. Walsh, C. L. Smith, G. Neri, G. F. Whitehead, C. M. Robertson and A. J. Cowan, *Faraday Discuss.*, 2015, **183**, 147.
35 J. J. Walsh, G. Neri, C. L. Smith and A. J. Cowan, *Chem. Commun.*, 2014, **50**, 12698.
36 Q. Zhang, D. Wang, X. Wei, T. Xie, Z. Li, Y. Lin and M. Yang, *Thin Solid Films*, 2005, **491**, 242.
37 J. P. Li, W. L. Chen, L. Chen, X. T. Zheng, G. S. Zhu and E. B. Wang, *Adv. Opt. Mater.*, 2018, **6**, 1800225.
38 I. D. Brown and D. Altermatt, *Acta Crystallogr., Sect. B: Struct. Sci.*, 1985, **41**, 244.
39 J. Zhao, J. Wang, J. Zhao, P. Ma, J. Wang and J. Niu, *Dalton Trans.*, 2012, **41**, 5832.
40 S. M. Liu, Z. Zhang, X. H. Li, H. J. Jia, M. W. Ren and S. X. Liu, *Adv. Mater. Interfaces*, 2018, **5**, 1801062.
41 H. Shi, Y. Yu, Y. Zhang, X. Feng, X. Zhao, H. Tan, S. U. Khan, Y. Li and E. Wang, *Appl. Catal., B*, 2018, **221**, 280.
42 J. Friedl, M. V. Holland-Cunz, F. Cording, F. L. Pfanschilling, C. Wills, W. McFarlane, B. Schricker, R. Fleck, H. Wolfschmidt and U. Stimming, *Energy Environ. Sci.*, 2018, **11**, 3010.
43 J. Xie, P. Yang, Y. Wang, T. Qi, Y. Lei and C. M. Li, *J. Power Sources*, 2018, **401**, 213.
44 B. Xu, L. Xu, G. Gao, Y. Yang, W. Guo, S. Liu and Z. Sun, *Electrochim. Acta*, 2009, **54**, 2246.
45 T. Akter, K. Hu and K. Lian, *Electrochim. Acta*, 2011, **56**, 4966.
46 D. M. Fernandes, M. P. Araújo, A. Haider, A. S. Mougharbel, A. J. S. Fernandes, U. Kortz and C. Freire, *Chemelectrochem*, 2018, **5**, 273.
47 V. A. Grigoriev, C. L. Hill and I. A. Weinstock, *J. Am. Chem. Soc.*, 2000, **122**, 3544.
48 J. Jia, Y. Zhang, P. Zhang, P. Ma, D. Zhang, J. Wang and J. Niu, *RSC Adv.*, 2016, **6**, 108335.
49 A. Tang, X. Wang, G. Xu, Z. Zhou and H. Nie, *Mater. Lett.*, 2009, **63**, 1439.
50 J. Yuan, L. Zheng and C. Hao, *RSC Adv.*, 2014, **4**, 39435.
51 Y. J. Jang, J. W. Jang, J. Lee, J. H. Kim, H. Kumagai, J. Lee, T. Minegishi, J. Kubota, K. Domen and J. S. Lee, *Energy Environ. Sci.*, 2015, **8**, 3597.
52 L. Jin, Y. Fang, P. Hu, Y. Zhai, E. Wang and S. Dong, *Chem. Commun.*, 2012, **48**, 2101.